



HAL
open science

Reconstruction of Coronary Arteries from One Rotational X-Ray Projection Sequence

Christophe Blondel, Grégoire Malandain, Régis Vaillant, Nicholas Ayache

► **To cite this version:**

Christophe Blondel, Grégoire Malandain, Régis Vaillant, Nicholas Ayache. Reconstruction of Coronary Arteries from One Rotational X-Ray Projection Sequence. [Research Report] RR-5214, INRIA. 2004, pp.43. inria-00077050

HAL Id: inria-00077050

<https://inria.hal.science/inria-00077050v1>

Submitted on 29 May 2006

HAL is a multi-disciplinary open access archive for the deposit and dissemination of scientific research documents, whether they are published or not. The documents may come from teaching and research institutions in France or abroad, or from public or private research centers.

L'archive ouverte pluridisciplinaire **HAL**, est destinée au dépôt et à la diffusion de documents scientifiques de niveau recherche, publiés ou non, émanant des établissements d'enseignement et de recherche français ou étrangers, des laboratoires publics ou privés.

Reconstruction of Coronary Arteries from One Rotational X-Ray Projection Sequence

Christophe Blondel — Grégoire Malandain — Régis Vaillant —

Nicholas Ayache

N° 5214

28 mai 2004

Thème BIO



*Rapport
de recherche*

Reconstruction of Coronary Arteries from One Rotational X-Ray Projection Sequence

Christophe Blondel* , Grégoire Malandain[†] , Régis Vaillant[‡] ,
Nicholas Ayache[§]

Thème BIO — Systèmes biologiques
Projets Chir et Epidaure

Rapport de recherche n° 5214 — 28 mai 2004 — 43 pages

Abstract: Cardiovascular diseases remain the first death cause in developed countries. In most cases, exploration of possibly underlying coronary artery pathologies is performed using injected X-ray coronary angiography imaging modality. Current clinical routine in coronary angiography is directly conducted in 2-D from angiograms acquired from several static points of view. However, for diagnosis and treatment purposes, coronary arteries reconstruction is highly suitable. In this report, we propose a novel method to reconstruct coronary arteries from one single rotational X-ray projection sequence. The purpose of this study is to provide physicians with a 3-D model of coronary arteries, *e.g.* for absolute tridimensional measures for lesion assessment, instead of direct projective measures deduced from the images, which are highly dependent on the point of view. Our method is split in 3 sequential steps: (1) 3-D stereoscopic reconstruction of coronary arteries centerlines, including respiratory motion compensation, (2) coronary arteries 4-D motion computation, and (3) 3-D tomographic reconstruction of coronary arteries, involving compensation for respiratory and cardiac motions. We have successfully tested it on the datasets from a synthetic phantom and 16 patients.

Key-words: Coronary angiography, Stereovision, Motion Analysis, Tomography

* INRIA, Action Chir, Sophia Antipolis, France

[†] INRIA, Projet Epidaure, Sophia Antipolis, France

[‡] General Electric Healthcare Europe, Advanced Medical Applications, Buc, France

[§] INRIA, Projet Epidaure, Sophia Antipolis, France

Reconstruction des artères coronaires à partir d'une séquence rotationnelle de projections rayons X

Résumé : Les maladies cardiovasculaires restent la première cause de mortalité dans les pays développés. Dans la plupart des cas, l'exploration d'une pathologie coronaires suspectée est réalisée par angiographie coronaire injectée. La routine clinique actuelle en angiographie coronaire est directement menée en 2D dans des angiogrammes acquis depuis différents points de vue statiques. Cependant, dans l'optique du diagnostic ou du traitement d'une lésion, la reconstruction des artères coronaires serait particulièrement bénéfique. Dans ce rapport, nous proposons une nouvelle méthode pour reconstruire les artères coronaires à partir d'une seule séquence rotationnelle de projections rayons X. Le but de cette étude est de fournir aux médecins un modèle 3D des artères coronaires. Ce modèle permet par exemple d'obtenir des mesures 3D absolues pour l'évaluation d'une lésion au lieu des mesures projectives directes effectuées dans les images, qui varient beaucoup selon le point de vue. Notre méthode est composée de trois étapes séquentielles : (1) reconstruction 3D stéréoscopique des lignes centrales des artères coronaires, prenant en compte le mouvement respiratoire, (2) estimation d'un mouvement 4D des artères coronaires, et (3) reconstruction tomographique 3D des artères coronaires, corrigeant les mouvements respiratoire et cardiaque. Nous avons testé avec succès cette méthode sur un jeu de données synthétiques et sur les données réelles acquises sur 16 patients.

Mots-clés : Angiographie coronaire, Stéréovision, Analyse de mouvement, Tomographie

1 Introduction

Cardiovascular diseases remain the major death cause in developed countries and will be the first worldwide death cause in 2008, according to World Health Organization. In particular, coronary artery lesions are involved in most cases of heart failure and are thus the subject of medical imaging examinations when a pathology is suspected.

To achieve adequate therapeutic orientation, 3-D measures such as absolute vessel sectional area would be of interest as they specify adapted diameter and length of angioplasty balloons or stents to be used. However, current clinical routine relies on direct analysis of images acquired from several static acquisitions from distinct points of view. It thus produces 2-D measures which suffer from well known point of view dependence, magnification factor, and superimposition effects. In this context, tridimensional reconstruction of coronary arteries would be of great clinical and diagnostic interest as it would provide physicians with 3-D absolute measures. Our purpose is thus to obtain tomographic reconstructions of coronary arteries, in a CT-like manner, from the most widely available imaging modality for coronary arteries examination: X-ray coronary angiography.

Reconstructing the coronary arteries still remains a very challenging task, despite the recent advances in medical imaging hardware and methodologies. In X-ray coronary angiography, the introduction of digital flat panel [RMV⁺02] combined with a rotational acquisition mode [KND02] allows for the proposal of new techniques in coronary arteries modeling. The main two difficulties that arise for the tomographic reconstruction of coronary arteries from angiograms are respiratory and cardiac motions that are visible in the X-ray projection sequence. In this report, we present a method that allows us to compute a volumic and dynamic reconstruction of coronary arteries from one single rotational X-ray projection sequence. To the opposite of iterative methods that alternates between motion estimation and tomographic reconstruction (*e.g.* [BKR⁺03]), the proposed method is direct and consists in three major steps: (1) a static 3-D reconstruction of coronary arteries centerlines at one given cardiac phase is performed, (2) this set of 3-D lines allows to estimate a 4-D motion, and (3) a 3-D tomographic reconstruction of coronary arteries is performed by integrating cardiac motion compensation.

The remainder of this report is organized as follows. In Section 2, we describe the new rotational acquisition protocol that was used and the datasets we were provided with. Section 3 details the 3-D centerlines reconstruction (which is coupled with respiratory motion correction), the coronary arteries motion estimation, and finally the tomographic reconstruction with motion compensation. Results on both synthetic and patient datasets are presented in Section 4, as well as some clinical applications enabled by the proposed methodology. Section 5 gives some future trends and perspectives.

2 Imaging protocol

Images were acquired on an Innova 2000 system, from General Electric Medical Systems. The angiograph model is equipped with a digital flat panel, which provides excellent contrast

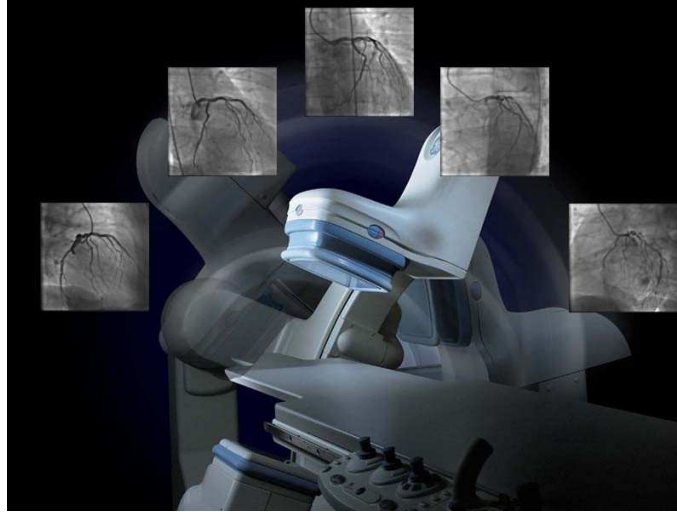


Figure 1: Rotational acquisition mode provides us with different points of view from one single angiogram sequence. Source: General Electric Medical Systems.

and dynamic range. These features are particularly suitable for acquisitions performed from a moving point of view.

Our acquisition protocol differs from the classical *static* acquisition routine. In our case, the gantry performs a rotation while acquiring the images. The gantry motion is characterized by constant SID (Source Intensifier Distance) value, constant CRA/CAU (Cranio/Caudal) angle value, and varying LAO/RAO (Left/Right Anterior Oblique) angle. Thus, the rotation occurs in patient axial plane, with maximum LAO/RAO angle amplitude from 120° to 200° .

Top rotation speed is 40° s^{-1} , leading from 3 to 5 seconds long acquisitions. Angiograph acquisition frame rate is 30 Hz. Thus, this protocol provides us with the imaging of 3 to 7 cardiac cycles. Images observing the same cardiac phase are approximately separated by 30° angular shift, depending on patient heart rate.

Figure 1 shows a schematic representation of images acquisition and the fact that the same cardiac phase can be observed from distinct points of view during the same acquisition run. For each patient, we have a single rotational sequence consisting in $\tilde{\mathcal{N}}'$ images I_n with spatial resolution 768×768 pixels and pixel size of 0.2 mm. We resampled these images into a 512×512 lattice for computational purposes. In addition, a precalibration step allowed to estimate the geometrical acquisition parameters that are summarized in $\tilde{\mathcal{N}}'$ projection matrix applications $\mathbf{M}_n : \mathbb{R}^3 \rightarrow \mathbb{R}^2$, the matrix \mathbf{M}_n being associated to image I_n .

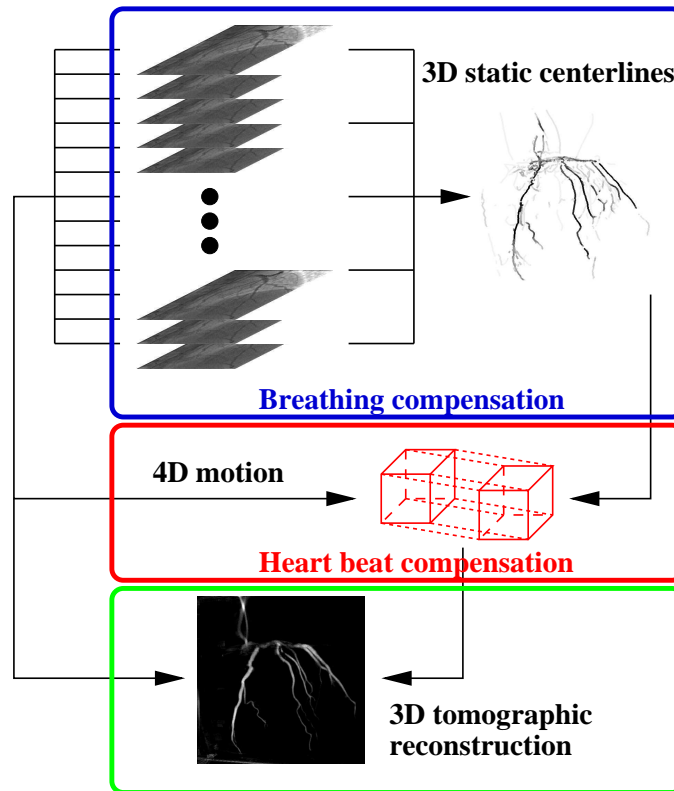


Figure 2: Overview of the main three steps of our method : static 3-D centerlines reconstruction, 4-D motion computation, and 3-D tomographic reconstruction.

3 Methods

A preprocessing step allows to estimate a pseudo-cardiac time for almost all the images of the sequence. The projection images, acquired at the same cardiac phase, but from different points of view allows both a static 3-D reconstruction of the coronary arteries centerlines and the respiratory motion estimation for these images. Propagating the respiratory motion estimation to the whole sequence allows to consider only the cardiac motion (assumed to be cyclic) that is computed from the complete set of projections, acquired at all cardiac phases. This motion is finally incorporated in a tomographic reconstruction stage, that is performed also with all the images of the sequence. Figure 2 summarizes these three subsequent algorithmic parts.

3.1 Preprocessing

A prerequisite for our method is the identification of a pseudo-cardiac time (or observed cardiac phase) for all images in the sequence. This information is computed from the image sequence information solely, without any external measures such as ECG signal. The basic idea is the following: along the cardiac cycle, systole is characterized by vessel contraction and a global top-to-bottom motion of the coronary tree in the axial direction, while diastole is characterized by vessel relaxation and a global bottom-to-top motion of the coronary tree in the axial direction. We assumed then that the resulting global vertical motion of coronary arteries in the image sequence is directly related to the cardiac phase.

To identify the vertical component of motion in the image sequence, we first compute for all images $I_n(x, y)$ the vector of line integrals $H_n(y) = \sum_x C_n(x, y)$ of the associated local contrast image $C_n(x, y)$ over the horizontal coordinate. The vertical motion between two successive frames is estimated by identifying the translation that minimizes the difference between the two vectors given by horizontal integrals. The process is iterated over the complete sequence and leads to a nearly periodic signal over time, whose high frequency characterizes the heart beat. Quasi synchronous images can be easily identified by either selecting image indices at local maxima of the integral signal, located at tele-diastole, or selecting image indices at local minima of the integral signal, located at tele-systole. In practice, quasi synchronous images acquired at tele-diastole are preferred because it corresponds to the most relaxed and stable state along heart motion, and consequently reduces superimpositions and potential asynchronism. The selected quasi synchronous images are called *reference images*. Figure 3 shows a typical example of the horizontal line integrals computation and illustrates the selection of quasi synchronous images in a rotational angiogram sequence.

Using reference images indices, we assign to each frame a *normalized time* that encodes the observed cardiac phase, relatively to cardiac phase in reference images. Normalized times vary in interval $[0, 1[$. The computation scheme is the following: two successive reference images are respectively assigned to normalized time $t = 0$ and normalized time $t = 1$, then normalized times of intermediate images are given by linear interpolation, as shown in Figure 4.

Time normalization is very convenient as it is adapted to cardiac period changes during the acquisition, which is often the case, as contrast agent acquisition usually accelerates heart motion. Indeed, we do not assume that the number of acquired images between two references times is fixed for a given sequence. However, images before the first and after the last reference images can not be assigned a normalized time. In the following, we discard these images from the sequence to only consider the \tilde{N} images, $\tilde{N} \leq \tilde{N}'$, between the first and last references images. The normalized time of image I_n is denoted t_n .

3.2 3-D centerlines reconstruction

The first stage of our method is the reconstruction of 3-D centerlines from the reference images, corresponding to normalized time $t = 0$. These images are selected from one single sequence and observe the same cardiac phase but from distinct points of view. Thus, they

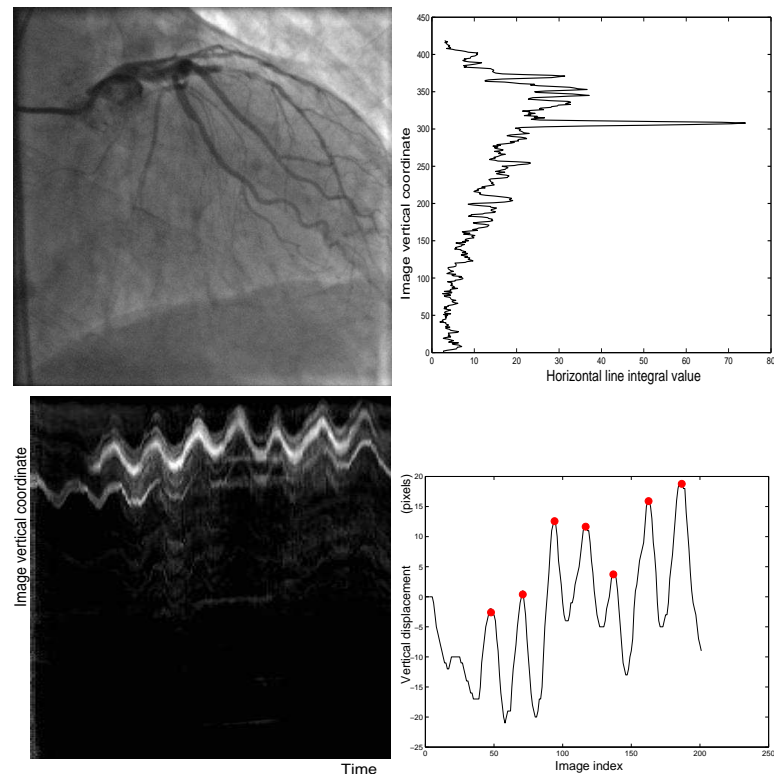


Figure 3: Quasi synchronous images selection according horizontal line integrals. Top: (left) an original angiogram $I_n(x, y)$, and (right) the plot of the associated horizontal line integrals $H_n(y)$. Bottom: (left) gathering all horizontal line integrals in an image exemplifies the cyclic cardiac motion, and (right) the vertical motion computed from difference minimization between successive horizontal line integrals, allowing for the selection of images, which are synchronous with respect to the cardiac cycle (spotted local maxima).

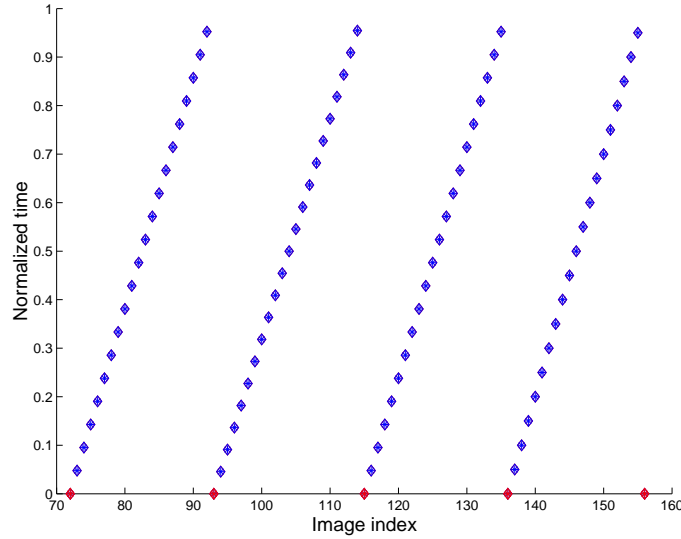


Figure 4: Normalized times computation: between two successive reference images, time is linearly interpolated between equivalent reference times $t = 0$ and $t = 1$. In this case, reference images are successively separated by 21, 22, 21 and 20 images.

are supposed to be uncorrupted by cardiac motion, but are subject to respiratory motion. The 3-D coronary artery centerline reconstruction is performed in four phases:

- vessel enhancement,
- coronary artery centerline extraction,
- artery centerline matching and 3-D reconstruction, and
- respiratory motion effect compensation.

3.2.1 Vessel enhancement

our first prerequisite is to enhance the vessels in the angiograms. We used the approach first proposed in [FNVV98, SNS⁺98] and extended in [KMA⁺00]. It relies on a multiscale Hessian-based filtering that enhances curvilinear structures.

For a given scale σ , original image I is first convoluted with a Gaussian kernel centered on pixel $p = (x, y)$, with standard deviation σ :

$$I(\sigma, p) = I(\cdot) * \mathcal{G}(\sigma, p, \cdot)$$

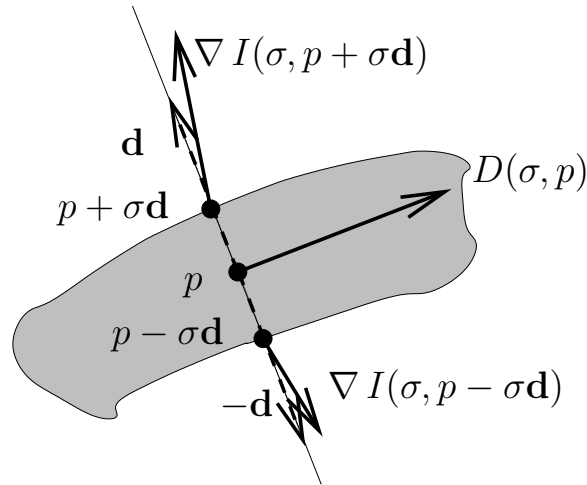


Figure 5: Filter response computation scheme. Filter response at pixel p is computed by calculating an edge response on both sides of the potential rectilinear structure, at distance σ from pixel p in direction \mathbf{d} orthogonal to the structure direction $D(\sigma, p)$.

The Hessian matrix of convoluted image is extracted:

$$\mathbf{H}(I, \sigma, p) = \begin{pmatrix} \frac{\partial^2 I(\sigma, p)}{\partial x^2} & \frac{\partial^2 I(\sigma, p)}{\partial y \partial x} \\ \frac{\partial^2 I(\sigma, p)}{\partial x \partial y} & \frac{\partial^2 I(\sigma, p)}{\partial y^2} \end{pmatrix}$$

The Hessian matrix gives the principal direction $D(\sigma, p)$ of a potential rectilinear structure at pixel p :

$$\tan(2D(\sigma, p)) = \frac{2 \frac{\partial^2 I(\sigma, p)}{\partial x \partial y}}{\frac{\partial^2 I(\sigma, p)}{\partial x^2} - \frac{\partial^2 I(\sigma, p)}{\partial y^2}}$$

If \mathbf{d} is a unitary vector which is orthogonal to principal direction $D(\sigma, p)$, the filter response is defined by:

$$R(\sigma, p) = \min \{ \nabla I(\sigma, p + \sigma \mathbf{d}) \cdot \mathbf{d}, \nabla I(\sigma, p - \sigma \mathbf{d}) \cdot (-\mathbf{d}) \}$$

Figure 5 shows an illustration of the filter response computation scheme.

This filter enhances rectilinear structures with width close to scale σ . Moreover, it also has maximum response at vessel center. Since the observed vessels observed have highly varying sizes, the previous computation is extended to multiple scales and conducted for a set of scales Σ , adapted for smallest to largest vessels. The best scale is selected according to the maximum filter response:

$$\sigma^* = \arg \max_{\sigma \in \Sigma} R(\sigma, x)$$

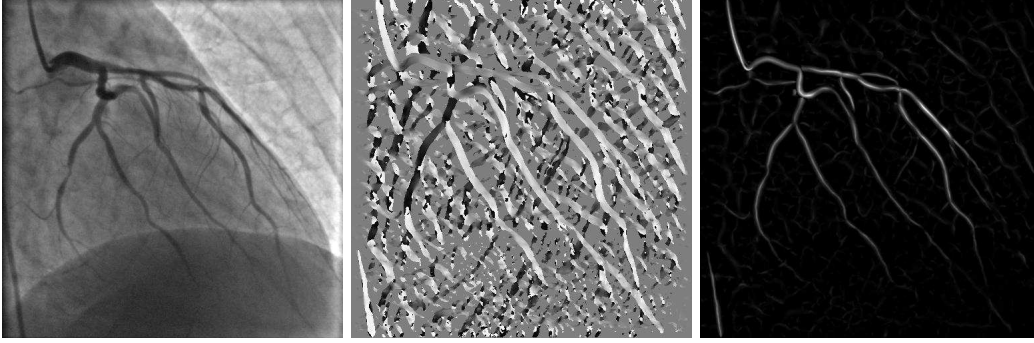


Figure 6: Multiscale filter analysis. From left to right: original angiogram, multiscale direction map, and multiscale filter response map.

The multiscale direction and filter response are given by:

$$D^*(x) = D(\sigma^*, x) \quad \text{and} \quad R^*(x) = R(\sigma^*, x)$$

In pixels length unit, for 512^2 spatial resolution images, we use $\Sigma = \{1, 2, \dots, 6\}$. Figure 6 shows the multiscale direction and filter response maps for an original angiogram. Multiscale filter response maps can be considered as a likelihood for pixels to belong to the projected centerline of a coronary artery, and will be extensively used in the next steps.

3.2.2 2-D centerlines extraction

from the above computed multiscale responses, we now build a set of 2-D curves that represent the coronary artery centerlines. This will be done in three steps:

- subpixelic local directional maxima computation,
- hysteresis thresholding of local directional maxima, and
- points linking.

Subpixelic local directional maxima computation in the multiscale response, we extract the pixels that are brighter than their two directional neighbors in the direction orthogonal to the potential rectilinear structure. Let p be a pixel and \mathbf{d} a unitary vector orthogonal to $D^*(p)$, subpixels that are used for comparison with pixel p are pixels at unit distance in \mathbf{d} direction, namely $p + \mathbf{d}$ and $p - \mathbf{d}$. A pixel p is a local directional maxima if the following conditions hold:

$$\begin{cases} R^*(p) > R^*(p + \mathbf{d}) \\ R^*(p) > R^*(p - \mathbf{d}) \end{cases}$$

A subpixelic estimation of the detected local maxima is achieved by fitting a quadric on points $(p - \mathbf{d}, R^*(p - \mathbf{d}))$, $(p, R^*(p))$, and $(p + \mathbf{d}, R^*(p + \mathbf{d}))$. Let us denote by $q(\alpha) = a\alpha^2 + b\alpha + c$ the quadric that approximates $R^*(p + \alpha\mathbf{d})$ and that verifies $q(-1) = R^*(p - \mathbf{d})$, $q(0) = R^*(p)$, and $q(1) = R^*(p + \mathbf{d})$. $q(\alpha)$ exhibits a maxima at $\hat{\alpha}$ with

$$\hat{\alpha} = \frac{R^*(p - \mathbf{d}) - R^*(p + \mathbf{d})}{2(R^*(p + \mathbf{d}) + R^*(p - \mathbf{d}) - 2R^*(p))}$$

The subpixelic position of the detected local maxima is then set to $p + \hat{\alpha}\mathbf{d}$. The extracted set of points contains most of the vascular but also many non vascular structures that have to be excluded.

Hysteresis thresholding most of the irrelevant local directional maxima, that do not correspond to vascular structures, are characterized by

- a low multiscale filter response and
- the small size of the connected components they belong to.

Hysteresis thresholding is perfectly adequate for this task. It requires a high and a low threshold. We compute these thresholds as quantiles of the cumulated histogram of the multiscale filter response maps over the complete sequence. The low threshold is set to a typical value of the multiscale filter response on vessels, while the high threshold is set to a typical value of the multiscale filter response on vessel centerlines. These quantiles can be related to relative area respectively occupied by vessels and vessels centerlines in the images. From our experiments, we chose the 90th percentile for the low threshold and the 98th percentile for the high threshold. In addition, hysteresis thresholding allows to retain only sufficiently large connected components. The minimal connected component size was set to 5 pixels. Figure 7 illustrates the effect of local directional maxima extraction and of hysteresis thresholding in an angiogram.

Points linking local directional maxima have been extracted point-wise, but vessels projected in images have a connected structure. We recover this structure by linking points that belong to the same component using the method described in [Gir87].

3.2.3 Multi-ocular matching

after linking, we have extracted, for all reference images, the 2-D centerlines of projected coronary arteries. Building correspondences between the centerlines of two reference images, acquired from two distinct points of view, allows for the tridimensional reconstruction of the coronary arteries centerlines by applying stereo-vision principles.

Most of proposed approaches for 3-D reconstruction of coronary arteries centerlines rely on only two angiographic views [MFLM98], typically obtained by biplane angiography. The rotational acquisition allows to get between 3 and 7 reference frames, depending on gantry

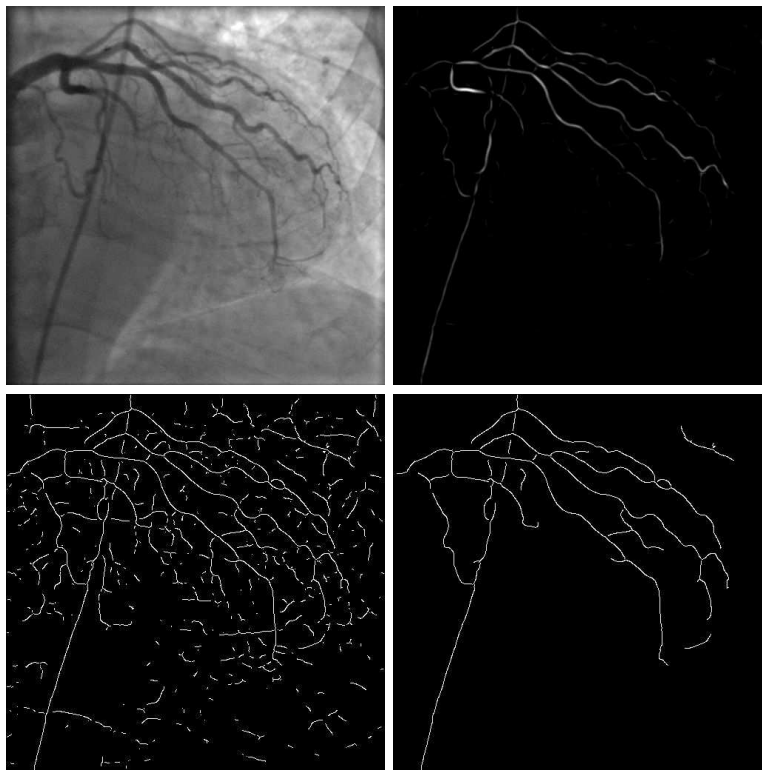


Figure 7: Hysteresis thresholding of local directional maxima. Top: (left) original angiogram, and (right) associated multiscale filter response map. Bottom: (left) extracted local directional maxima subpixels set, and (right) retained centerlines after hysteresis thresholding.

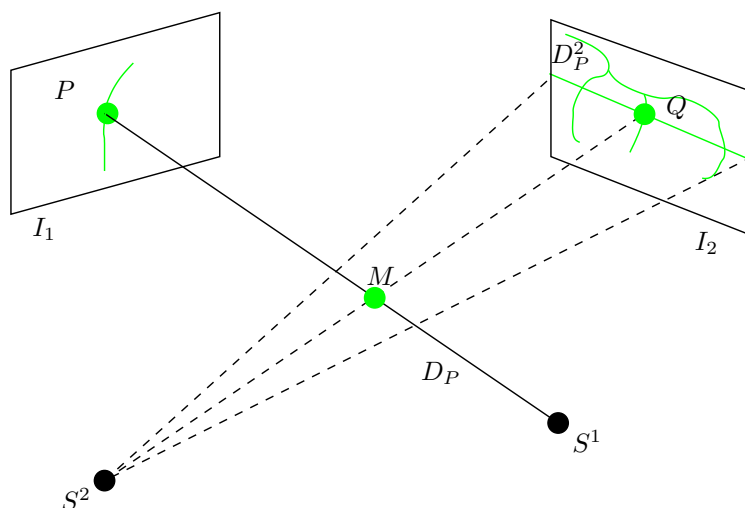


Figure 8: Epipolar constraint in two images. 3-D point M projects as P in image 1. Consequently, the projection Q of M in I_2 , that matched P , is located on the projection D_P^2 of line D_P on I_2 .

rotation speed and on patient heart rate. We propose to use all the available images to perform a multi-ocular matching of the extracted centerlines in reference images, as basically described in [BVD⁺02]. This is achieved by optimizing a matching criterion detailed below.

Asymmetric matching let us first consider the asymmetric problem that consists in matching a set of linked points, denoted by (P_1, \dots, P_C) , in a first image, say I_1 , with the extracted centerlines in a second image, I_2 .

- ▷ Problem formulation: As illustrated by Figure 8, a point P in I_1 is the projection of a 3-D point M located in 3-D line D_P , joining source position S^1 to projection position P . The projection of the 3-D line D_P in I_2 , denoted D_P^2 , must contain the projection Q of M in I_2 : this is the *epipolar constraint*.

Unfortunately, the epipolar constraint does generally not yield a single match in I_2 for each $P \in I_1$. Indeed, in most cases, line D_P^2 intersects more than one centerline in I_2 , resulting in a set of matching candidates in I_2 (see Figure 8). Our experiments shows an average of 5 matching candidates per point: Figure 9 displays the histogram of the number of matching candidates, when browsing all points in extracted centerlines set of one image.

Let \mathcal{Q}_i denote the set of matching candidates in I_2 for point P_i in I_1 . Building the correspondences for a set of linked points (P_1, \dots, P_C) of I_1 consists then in choosing a set of points $\{Q_1, \dots, Q_C\} \in \mathcal{Q}_1 \times \dots \times \mathcal{Q}_I$.

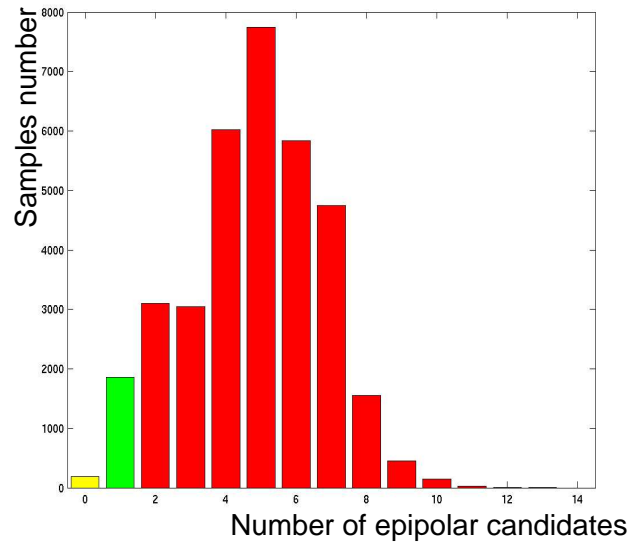


Figure 9: Typical histogram of the number of matching candidates under epipolar constraint. Even if some point do not have any corresponding candidate (in yellow), and some points have only one candidate (in green), most of points have two or more candidates (in red). In this case, there are in average 4.8 candidates under epipolar constraint for each point to be matched.

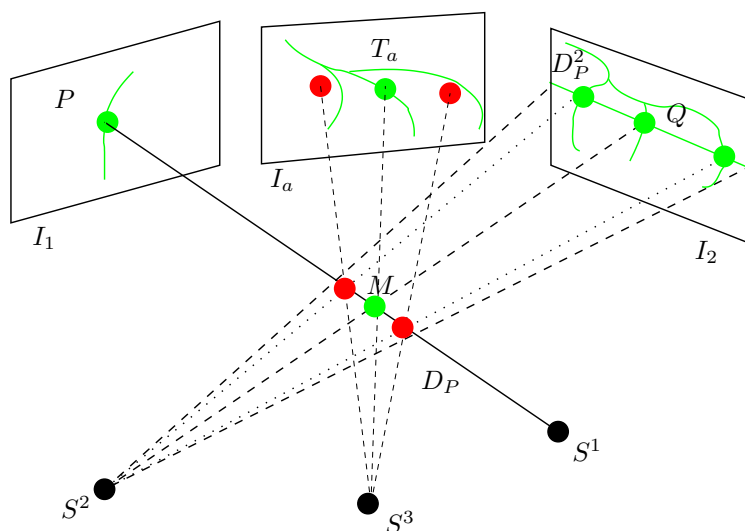


Figure 10: Epipolar constraint in three images. Among the three possibly reconstructed 3-D points, only one projects on a vessel in the additional image I_a , at position T_a . Thus, the corresponding matching candidate Q in I_2 is more likely to be the correct matching point for P in I_1 .

To compare different matching configuration, we now design a criterion to measure the quality of a given matching hypothesis $(P_i, Q_i)_{i=1\dots C}$. This quality measure is made of two parts:

- an external energy term, involving reference images information, and
 - an internal energy term, favorizing intrinsically coherent matching configurations.
- ▷ External energy term: To disambiguate between the matching candidates, the reference images other than I_1 and I_2 are used. This additional information is indeed useful: among the several matching candidates given by the epipolar constraint, only one will be coherent with the additional views in most cases. As shown in Figure 10, to each epipolar candidate corresponds a 3-D point using stereoscopic reconstruction, whose projection in additional images is on a vessel only for the correct correspondence.

A numerical criterion that reflects the relevance of a reconstructed 3-D point is the value of the multiscale filter response of its projection in the additional views. Let \mathcal{A} denote the set of indices of additional views, of cardinal \tilde{A} . To any given matching pair (P, Q) corresponds a 3-D reconstructed point M , whose projection in additional image with index $a \in \mathcal{A}$ is denoted T_a . We recall that R_a^* is the multiscale filter response map associated to the additional image of index a . Then, the external energy term

measuring matching pair (P, Q) quality is given by:

$$E_1(P, Q) = \frac{1}{\mathcal{A}} \sum_{a \in \mathcal{A}} R_a^*(T_a)$$

This criterion reaches high values for matching pairs that are coherent with additional reference images.

- ▷ Internal energy term: the above criterion is convenient for points, but did not take into account the intrinsic linked structure of vessel centerlines. Indeed, a linked set of points in image I_1 , that represents a detected centerline, is more likely to project as a single connected component in other reference images than as disconnected pieces. Exceptions may occur in case of superimposition or defective centerlines extraction. This constraint is called *geometrical coherence*.

Let (P_1, Q_1) and (P_2, Q_2) denote two successive matching pairs, where P_2 follows P_1 in a set of linked points in the extracted centerline in I_1 . We define the penalty for two successive matching point pairs as a function of the distance $\|Q_1 Q_2\|$:

$$E_2((P_1, Q_1), (P_2, Q_2)) = \mathcal{P}(\|Q_1 Q_2\|)$$

with

$$\mathcal{P}(d) = \begin{cases} 0, & \text{if } d \leq \mathcal{D}_l \\ \frac{d - \mathcal{D}_l}{\mathcal{D}_h - \mathcal{D}_l}, & \text{if } \mathcal{D}_l < d < \mathcal{D}_h \\ 1, & \text{else} \end{cases}$$

Thresholds \mathcal{D}_l and \mathcal{D}_h are chosen such that matched points whose distance is below \mathcal{D}_l are not penalized, and such that the ones whose distance is above \mathcal{D}_h are not over-penalized since they may indicate a discontinuity in the matching points sequence. Typically, $\mathcal{D}_l = 2$ pixels and $\mathcal{D}_h = 50$ pixels for 512^2 images.

- ▷ Matching criterion: Finally, the criterion measuring the quality of a matching configuration $(P_i, Q_i)_{i=1 \dots C}$ is given by the weighted sum of the external energy term for all points pairs and of the internal energy term for all successive points pairs:

$$C((P_i, Q_i)_{i=1 \dots C}) = - \sum_{i=1 \dots C} E_1(P_i, Q_i) + \alpha \sum_{i=1 \dots C-1} E_2((P_i, Q_i), (P_{i+1}, Q_{i+1}))$$

The optimal set of correspondences, $\{\hat{Q}_1, \dots, \hat{Q}_C\} = \arg \max C((P_i, Q_i)_{i=1 \dots C})$, is computed by a dynamic programming based approach [Dij59], which enables to find the global optimum in predictable time and low computational complexity.

This optimization is repeated for all sets of linked points of image I_1 . Figures 11 and 12 show an example of results provided by matching process. The sum of the above matching criterion over all the sets of linked points in I_1 is assumed to be a quality measure of the 3-D reconstruction of all vessels centerlines: we call it the *global asymmetric matching criterion*.

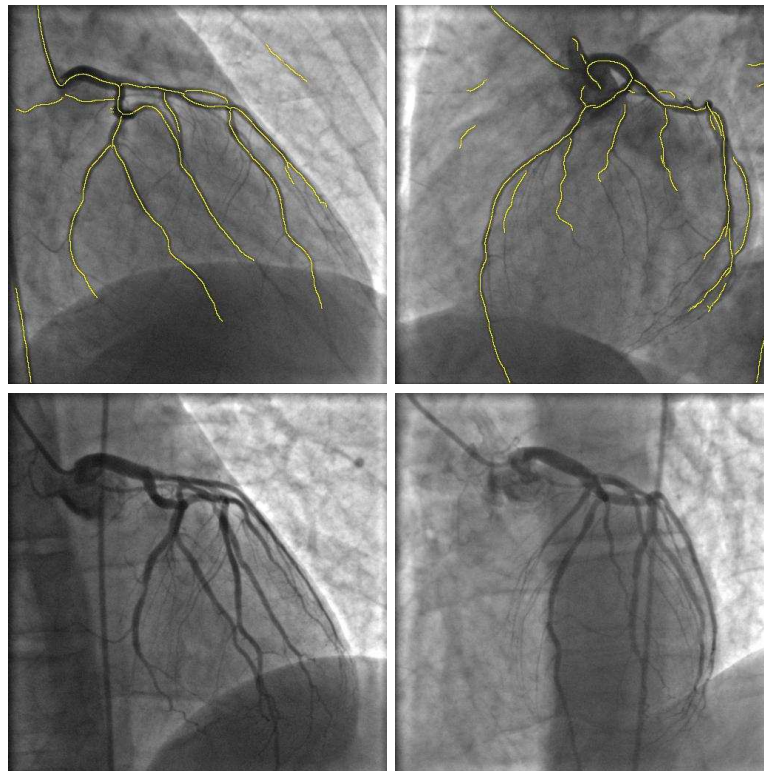


Figure 11: Reference frames for dynamic programming. Centerlines in the first reference image (top left) are matched with centerlines in the second reference image (top right), according to the information contained in the two additional views (bottom).

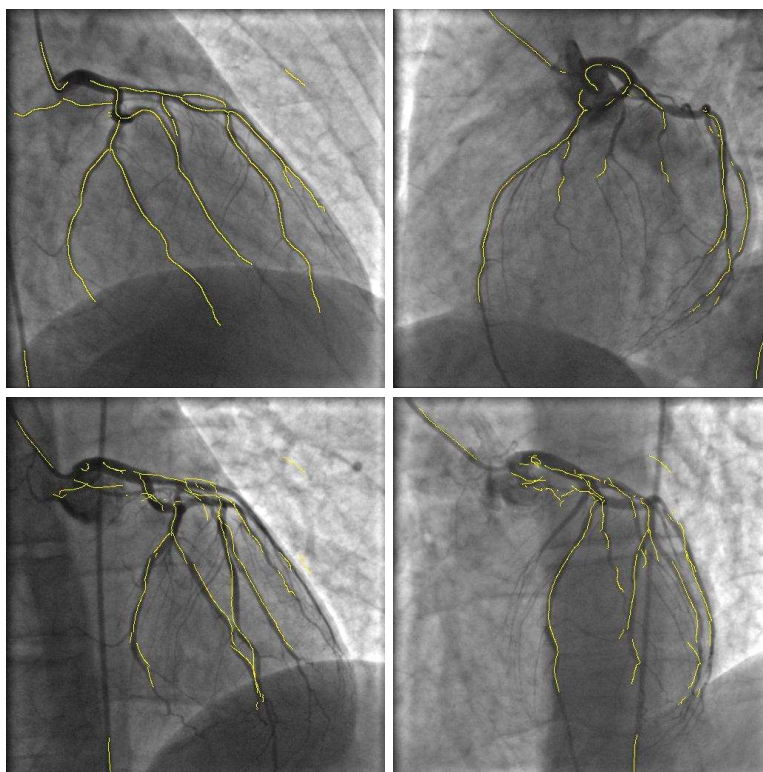


Figure 12: Results of the dynamic programming based matching process. Projection of the 3-D reconstructed points is presented in all reference images.

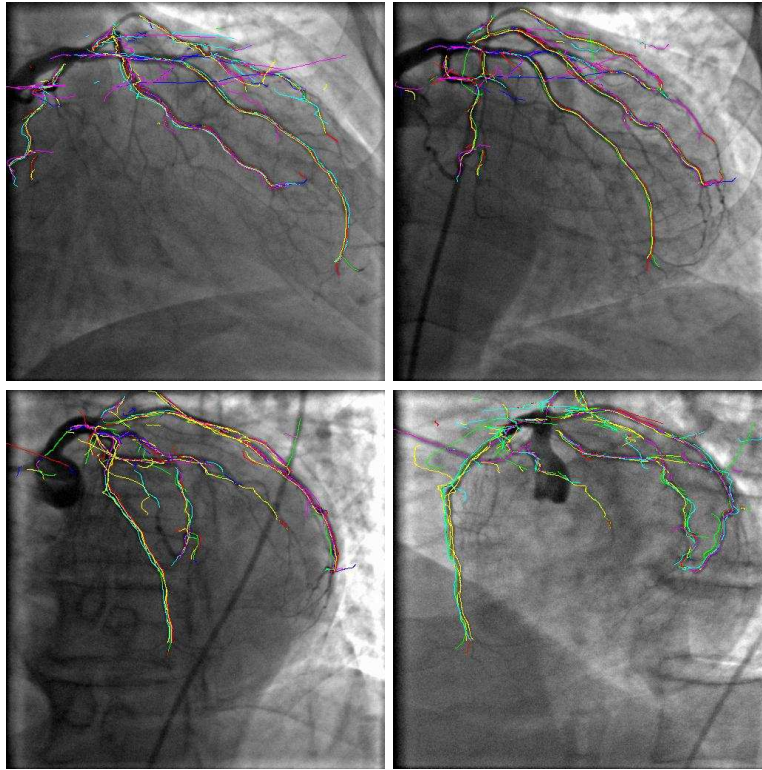


Figure 13: Symmetric reconstruction. Projection in four reference images of the centerlines reconstructed by considering all the ordered pairs of reference images, (a different color is associated with each asymmetric reconstruction). 3-D centerlines reconstructions appear redundant and slightly shifted.

Matching symmetrization the above described reconstruction method is intrinsically asymmetric. Centerlines in image I_1 are matched with centerlines in image I_2 according to remaining images, and the result depends on the choice of both images I_1 and I_2 which is undesirable.

A *symmetric* reconstruction is then achieved by considering all ordered pairs of images among the reference images. With our notations, it comes to consider $(\tilde{A}+2)(\tilde{A}+1)$ pairs of images. This yields a number of 3-D reconstructed centerlines. The ones that are supposed to represent the same 3-D vessel may be slightly shifted from each other, mainly because of the respiratory motion, but also of an imperfect synchronization of reference images and of geometrical reconstruction errors.

Figure 13 shows the result of this symmetric reconstruction. The *global matching cri-*

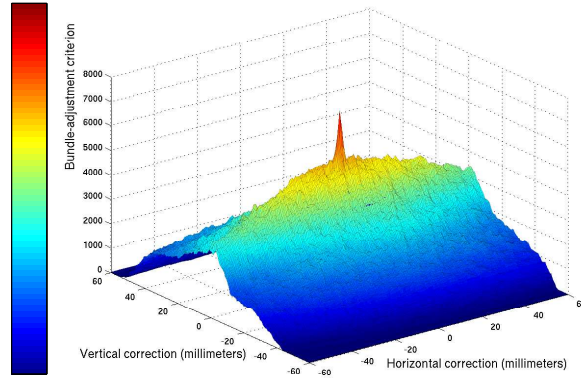


Figure 14: Global matching criterion value with respect to vertical and horizontal translations of one of the reference images. A maximum clearly occurs at the correct image translation.

terion after symmetrization is merely given by the sum of all *global asymmetric matching criteria* over all ordered pairs of reference images.

Respiratory motion compensation as shown in [WRE95, HGE98, DSB⁺99, KGYF02], the respiratory motion effect on coronary arteries position can be approximated by a 3-D translation, mainly in the axial direction. From the acquisition point of view, it corresponds to a translation of the images in their acquisition plane, that can be encoded in the calibration parameters, *i.e.* in the M_n matrices. Thus, compensating for the respiratory motion can be achieved by re-estimating these calibration matrices. Indeed, as shown in Figure 14, the global matching criterion reaches its maximum for optimal calibration parameters.

We thus consider optimizing the global matching criterion with respect to the cameras translation in their acquisition plane, in order to estimate the respiratory motion. As a side effect, it will also improve the quality of the 3-D reconstructed centerlines.

To optimize the global matching criterion, we use a FSQP optimization method implementation [LZT97, LT01]. It results in a translational correction in acquisition plane for reference images, reflecting respiratory motion effect. We propagate this information to other than reference images by linearly interpolating corrections that were found for the two surrounding reference frames.

Reconstructions fusion the respiratory motion compensation improved the reconstruction of 3-D centerlines, particularly by decreasing the slight shift observed between asymmetric reconstructions, but is not sufficient to yield a *perfect* superimposition of the 3-D centerlines obtained from the different asymmetric reconstruction. Keeping multiple reconstructions of the same 3-D vessels may bias the forthcoming 4-D motion estimation since

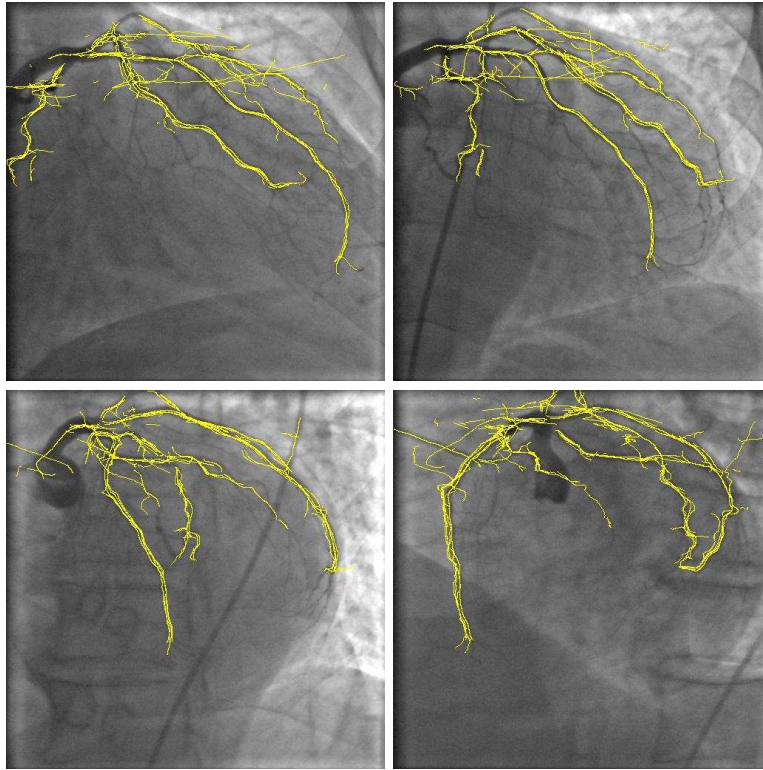


Figure 15: Fusion of redundant 3-D reconstructed centerlines sets. Projection in the four reference images of the reconstructed centerlines before applying the fusion process is presented. Geometrical redundancy appear clearly.

it introduces spatial imprecision. Consequently, we fuse the distinct reconstructed centerlines sets in a single set where formerly redundant points appear only once. We also store redundancy information, as it is a useful indicator for confidence in reconstructed points.

The fusion relies on a threshold representing the maximum shift distance allowed for redundant points. We chose it equal to 5 millimeters which is an approximate value for largest observable coronary arteries diameter. Two 3-D centerlines sets are fused in a geometrical manner: for each point in the first set, we find the closest point in the second set, if their distance is smaller than a distance threshold, then points are considered redundant and are replaced by their barycenter, else the closest point is added as a new point. Iterating this process for all 3-D reconstructed centerlines sets leads to a fused 3-D centerlines reconstruction. Figures 15 and 16 illustrates the effect of fusion on redundant 3-D reconstructed centerlines sets.

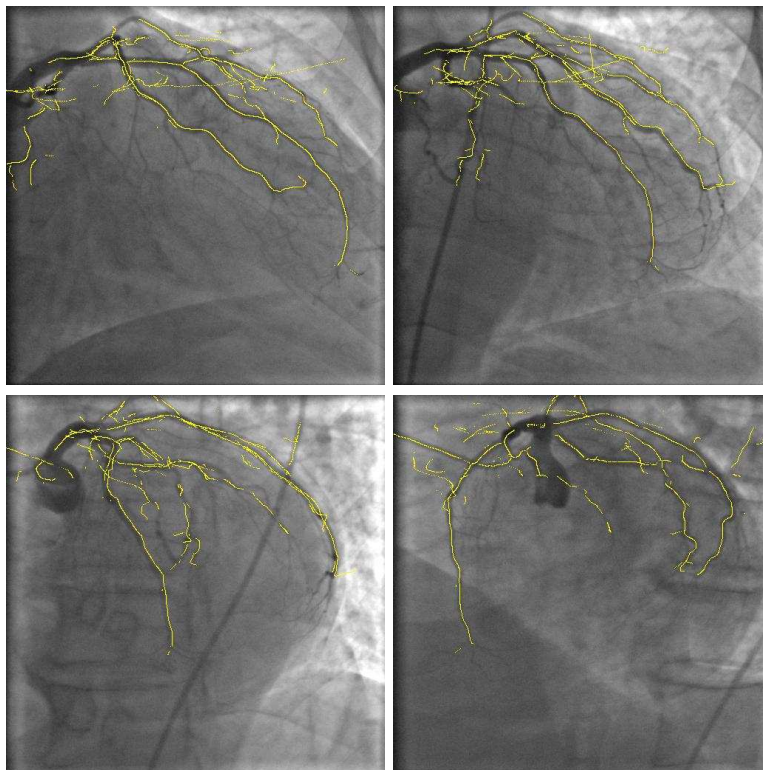


Figure 16: Fusion of redundant 3-D reconstructed centerlines sets. Projection in the four reference images of the reconstructed centerlines after applying the fusion process. In most of the cases, geometrical redundancy is removed, a *geometrically average* reconstruction has been built.

Additionally, redundancy of fused points is given by the number of redundant points that contributed to the fused point position. In practice, we build an application $\Lambda : \mathcal{X} \rightarrow \mathbb{R}$, which associates its redundancy $\Lambda(X)$ to any point X in the fused 3-D centerlines set \mathcal{X} . $\Lambda(X)$ can be interpreted as the confidence value for point X .

As the end of this first stage, we have 3-D reconstructed centerlines, including confidence indices, that have been corrected from respiratory motion effect. This reconstruction was obtained from a few images, which are quasi synchronous with respect to the cardiac cycle.

3.3 4-D motion computation

From above computations, a 3-D reconstruction of the coronary arteries centerlines at the cardiac reference time is obtained, as well as the respiratory motion compensation for all the rotational sequence images. This 3-D model will now be used to estimate the cardiac motion.

Contrary to 3-D motion approaches usually involved in the biplane case [RBCC94, SDQ⁺03], that estimate a 3-D motion from time to time, we use simultaneously all frames, independently from the cardiac phase at which they were acquired, to estimate a global motion, parameterized over space and time, hence called 4-D motion.

3.3.1 Motion parameterization

to choose a motion parameterization, we recall some features of coronary arteries motion:

- spatial smoothness,
- temporal smoothness, and
- semi-local spatial and temporal influence.

These characteristics led us to choose a parameterization based on 4-D B-solid, which is a 4-D tensor product of B-splines. This parameterization is a generalization of 3-D B-solids proposed in [RAH97] and has the three formerly described properties, derived from B-splines construction.

Extremal space coordinates are computed from the bounding box of the 3-D centerlines set \mathcal{X} . From our experiments, the spatial support was sampled using spatial control points not successively distant of more than 2 centimeters. Time extremal values are merely given by the interval $[0, 1[$. This interval is sampled using 10 control points. In practice, we used cubic B-splines, providing a sufficient number of degrees of freedom. Knots vectors on space coordinates are chosen open uniform. This allows one of the B-spline basis functions to be non null on the spatial bounds of the motion, and thus the motion may be non null on the spatial bounds of the motion support. On the opposite, knots vector in time coordinate is chosen uniform. This properties enforces all B-spline basis functions to be null on the temporal bounds, and thus the motion is constrained to be null at equivalent reference times $t = 0$ and $t = 1$.

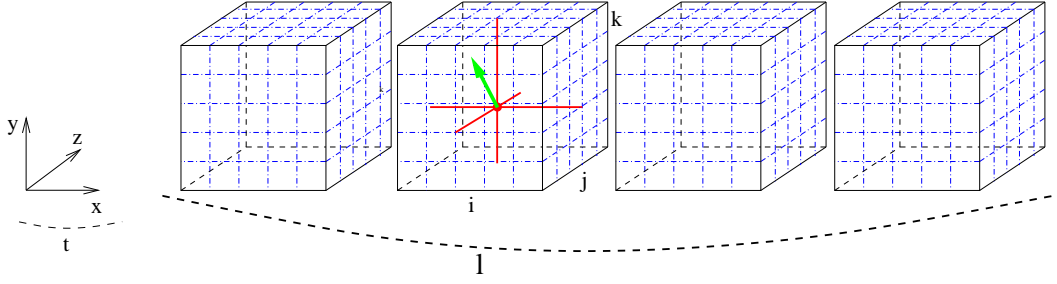


Figure 17: A 4-D B-solid is determined by tridimensional vectors \mathbf{p}_{ijkl} at all control points in the 4-D tensor structure, given by space indices i , j , and k and time index l .

Sets \mathcal{I} , \mathcal{J} , and \mathcal{K} respectively discretize x , y , and z space coordinates, set \mathcal{L} discretizes time coordinate. Their respective cardinals are $\tilde{\mathcal{I}}$, $\tilde{\mathcal{J}}$, $\tilde{\mathcal{K}}$, and $\tilde{\mathcal{L}}$. Under a 4-D B-solid motion $\Phi : \mathbb{R}^p \times \mathbb{R}^3 \times \mathbb{R} \rightarrow \mathbb{R}^3$, parameterized by vector $\mathbf{p} \in \mathbb{R}^p$, the position of point $X = (x, y, z)$ after the application of the motion, evaluated at normalized time t , is given by:

$$\Phi(\mathbf{p}, X, t) = X + \sum_{ijkl} B_i(x)B_j(y)B_k(z)B_l(t)\mathbf{p}_{ijkl}$$

Figure 17 shows a schematic representation of 4-D B-solid motion parameterization.

3.3.2 Motion optimization

estimating the heart motion comes now to find the optimal parameters vector $\hat{\mathbf{p}}$ that will *explain* at best the 2-D displacements observed in images I_n . This will be achieved through the optimization of a criterion that aims to quantitatively evaluate the coherency of a 4-D B-solid motion $\Phi(\mathbf{p}, \cdot, \cdot)$ with the angiogram sequence, through an external energy term, and that penalizes degenerate motions, through a regularization term.

The multiscale filter response, R_n^* , is considered as a likelihood for pixels to belong to an artery projection. Summing the values of these responses for the projected 3-D reconstructed points X under motion yields to the external energy term $\Psi : \mathbb{R}^p \mapsto \mathbb{R}$ of the criterion:

$$\Psi(\mathbf{p}) = \frac{1}{\tilde{\mathcal{N}}\tilde{\Lambda}} \sum_{n \in \mathcal{N}} \sum_{X \in \mathcal{X}} \Lambda(X) R_n^*(\mathbf{M}_n(\Phi(\mathbf{p}, X, t_n))) \quad \text{with} \quad \tilde{\Lambda} = \sum_{X \in \mathcal{X}} \Lambda(X)$$

where \mathcal{X} denotes the set of 3-D reconstructed points. It has to be pointed out that the multiscale filter response of projected point X is weighted by its reconstruction confidence $\Lambda(X)$.

Successive steps for the evaluation of external energy term of the criterion are:

- motion application $\Phi : \mathbb{R}^p \times \mathbb{R}^3 \times \mathbb{R} \mapsto \mathbb{R}^3$,
- projection application $\mathbf{M}_n : \mathbb{R}^3 \mapsto \mathbb{R}^2$,

- multiscale filter response value $R_n^* : \mathbb{R}^2 \mapsto \mathbb{R}$, and
- weighting by confidence index $\Lambda : \mathcal{X} \subset \mathbb{R}^3 \rightarrow \mathbb{R}$.

The gradient vector of Ψ can be computed analytically:

$$\frac{d\Psi(\mathbf{p})}{d\mathbf{p}} = \frac{1}{\tilde{N}\tilde{\Lambda}} \sum_{n,X} \Lambda(X) \frac{dR_n^*}{d\mathbf{M}_n} \frac{d\mathbf{M}_n}{d\Phi} \frac{\partial\Phi(\mathbf{p}, X, t_n)}{\partial\mathbf{p}}$$

To prevent from degenerated optimal motions, we add internal energy terms which penalize motions with large amplitude, motions with erratic spatial behavior, and motions with erratic temporal behavior.

To estimate the motion amplitude, we evaluate the normalized sum over the control points of the square norm of vectors \mathbf{p}_{ijkl} :

$$\Gamma_1(\mathbf{p}) = \frac{1}{\tilde{I}\tilde{J}\tilde{K}\tilde{L}} \sum_{ijkl} \|\mathbf{p}_{ijkl}\|^2$$

To estimate the motion smoothness, we evaluate the normalized sum over the control points of the square norm of the vector difference between \mathbf{p}_{ijkl} and its spatial neighbors \mathcal{V}_{ijkl}^X (in terms of 26-connectivity in 3-D) and its temporal neighbors \mathcal{V}_{ijkl}^t (in terms of 2-connectivity in 1D):

$$\Gamma_2(\mathbf{p}) = \frac{1}{\tilde{I}\tilde{J}\tilde{K}\tilde{L}} \sum_{ijkl} \frac{1}{\tilde{\mathcal{V}}_{ijkl}^X} \sum_{i'j'k'l' \in \mathcal{V}_{ijkl}^X} \|\mathbf{p}_{ijkl} - \mathbf{p}_{i'j'k'l'}\|^2$$

$$\Gamma_3(\mathbf{p}) = \frac{1}{\tilde{I}\tilde{J}\tilde{K}\tilde{L}} \sum_{ijkl} \frac{1}{\tilde{\mathcal{V}}_{ijkl}^t} \sum_{ijk'l' \in \mathcal{V}_{ijkl}^t} \|\mathbf{p}_{ijkl} - \mathbf{p}_{ijk'l'}\|^2$$

where $\tilde{\mathcal{V}}_{ijkl}^X$ and $\tilde{\mathcal{V}}_{ijkl}^t$ are the respective cardinals of sets \mathcal{V}_{ijkl}^X and \mathcal{V}_{ijkl}^t .

The final criterion for 4-D motion optimization is:

$$\Upsilon(\mathbf{p}) = \Psi(\mathbf{p}) - \alpha_1\Gamma_1(\mathbf{p}) - \alpha_2\Gamma_2(\mathbf{p}) - \alpha_3\Gamma_3(\mathbf{p})$$

Knot vectors properties and discretization scheme lead to approximately 10 degrees of freedom along each coordinate, a degree of freedom being a tridimensional vector. Thus, vector \mathbf{p} typically has 30000 components. Consequently, optimizing the criterion requires a method dedicated to very large scale nonlinear optimization problems. We chose the Polak-Ribière variant of the nonlinear conjugate gradient algorithm [GMW82] and used the CONMIN implementation described in [Van73]. Optimization process leads to an optimal parameterization $\hat{\mathbf{p}}$ and associated optimal motion $\Phi(\hat{\mathbf{p}}, \cdot, \cdot) : \mathbb{R}^3 \times \mathbb{R} \rightarrow \mathbb{R}^3$ that will further simply be denoted by Φ . The motion $\Phi(t, \cdot) : \mathbb{R}^3 \rightarrow \mathbb{R}^3$ for a given normalized time t is denoted Φ_t . Figures 18 and 19 present the comparative results for motion computation by comparing 3-D centerlines projection before and after 4-D motion application.

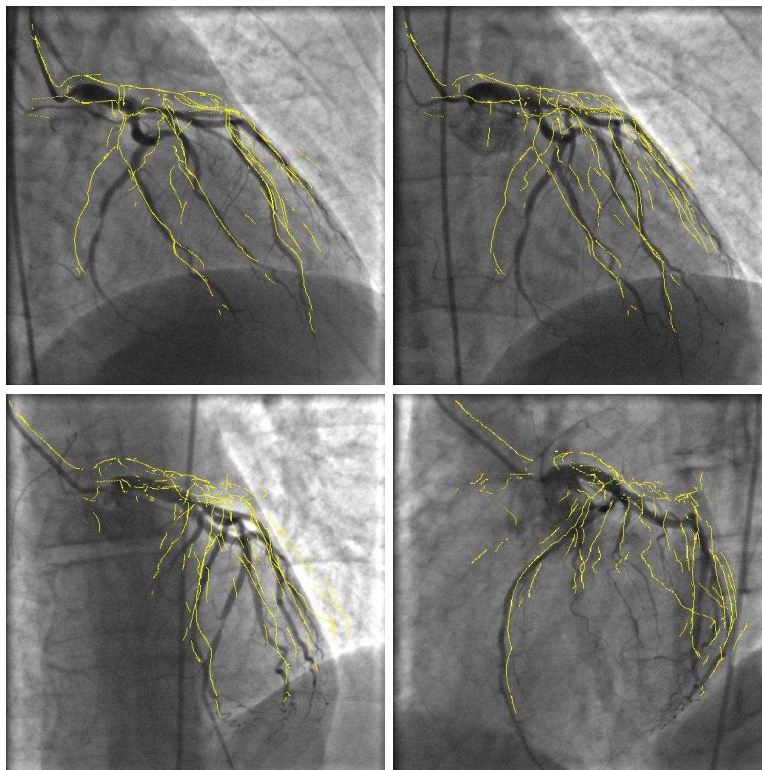


Figure 18: Results for 4-D motion computation. Projection in four images (acquired at four distinct normalized times, all differing from the reference time) of the 3-D centerlines reconstruction before 4-D motion application. The shift of coronary arteries due to motion is clearly visible.

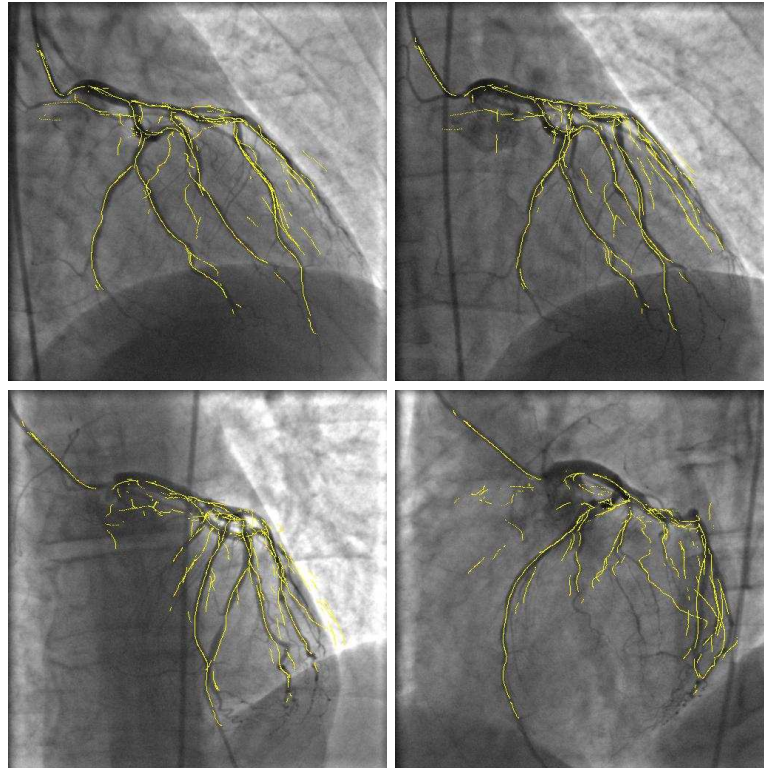


Figure 19: Results for 4-D motion computation. Projection in the same four images (figure 18) of the 3-D centerlines reconstruction after 4-D motion application. According to centerlines superimposition on vessels, 4-D motion has been correctly determined by the optimization process.

3.4 3-D tomographic reconstruction

In our context, datasets differ from ideal tomographic conditions in two points:

- data truncation for background structures that are located far from the gantry rotation center and
- coronary arteries motion occurring during the acquisition.

3.4.1 Background removal

due to the imaging protocol, structures that are too far from the gantry rotation center are not visible in the complete sequence. This mainly applies to non vascular structures that are located in the background. To deal with this truncation issue, we simulated subtracted angiograms. Indeed, a rotational acquisition without contrast agent injection that perfectly superimposes with a injected sequence, allowing subtracted angiography, is unrealistic. This limitation comes from the impossibility of synchronizing the three motions that occur during the acquisition:

- gantry rotation,
- respiratory motion, and
- cardiac motion.

Thus, we have to produce virtual mask angiograms from original angiograms. This is done image-wise in four steps:

- binary vessel detection,
- virtual background image computation,
- virtual mask image computation, and
- virtual subtracted image computation.

The first step is done by applying an hysteresis thresholding to the multiscale filter response maps. The low and high thresholds are chosen equal to those used during centerlines detection. To manage potential detection defects near the bifurcations or at distal parts of coronary arteries, this binary image is dilated using mathematical morphology [Ser82].

The second step is achieved by applying a morphological closure to the original image [Ser82], this leads to an approximation of the corresponding image, acquired without contrast agent injection.

The third step is performed combining these two images in the following way: for any pixel, its virtual mask image value is given by the virtual mask image value, if the pixel belongs to a vessel according to the binary vessel detector image, or by the original image value, if the pixel does not belong to a vessel. This third image is a virtual mask of the original image.

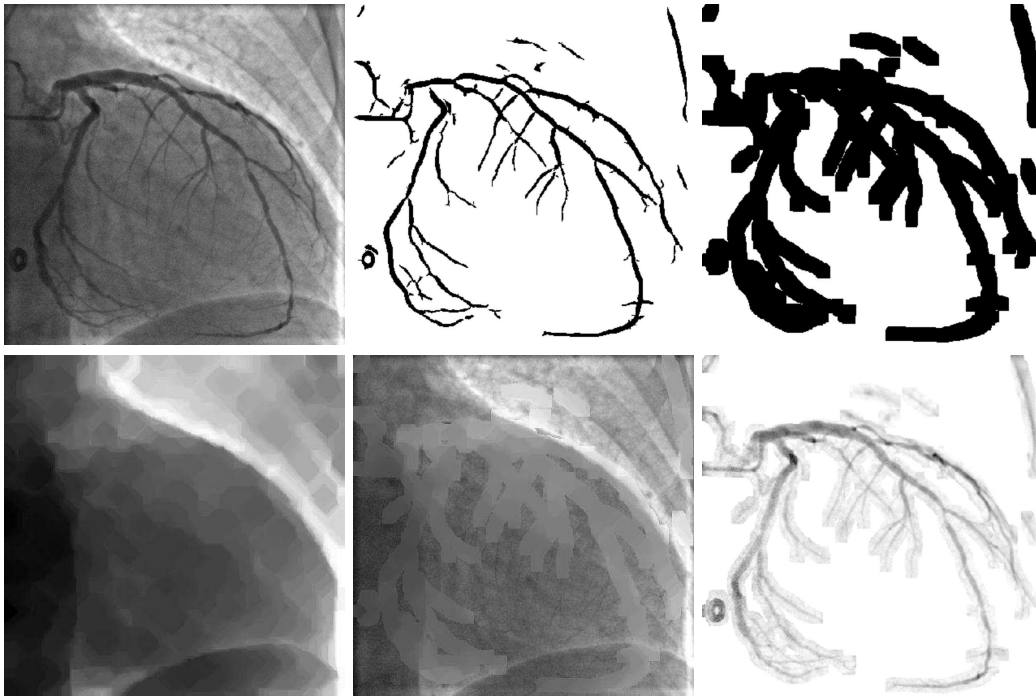


Figure 20: Virtual subtraction of angiograms. Top, from left to right: original angiogram, binary image of vessel detector, and dilated binary vessel detector. Bottom, from left to right: virtual background image obtained from morphological closure, virtual mask image combining vessel detector information and original and virtual mask images, and virtually subtracted image. Subtraction process removes most of non vascular background structures, that are subject to truncation, while preserving vessels information.

The last step is the logarithmic subtraction of the original image I_n and the virtual mask image to produce the virtually subtracted image J_n that will be actually used as tomographic data. Figure 20 illustrates the virtual subtraction process.

3.4.2 Motion compensation

classical tomographic reconstruction methods make the hypothesis that the observed object remains still during sinogram acquisition, which is of course not the case for coronary angiography. Many approaches propose to restraint the sinogram to the angiograms that were acquired at given cardiac phase [RGK⁺02] or to phases that remain close to a reference phase [MRV⁺03]. This leads to few views tomographic reconstructions and often suffers from strong artifacts due to data lack.

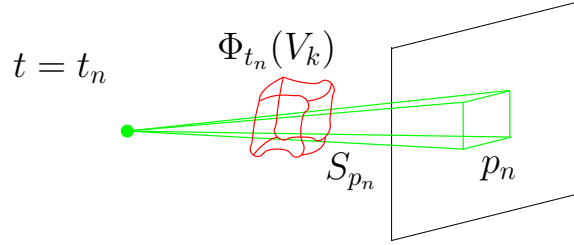


Figure 21: Contribution of voxel V_k , considered at normalized time $t = 0$, to pixel p_n , considered at normalized time $t = t_n$ is given by the volume of the intersection between solid angle S_{p_n} and deformed voxel $\Phi_{t_n}(V_k)$ at time $t = t_n$.

On the contrary, we use all available frames, homogeneously and independently from the cardiac phase they observe. In [BKR⁺03], the authors propose an iterative scheme alternating between motion estimation and tomographic reconstruction, in the CT context. On the opposite, we use a *single-pass* reconstruction method. The tomographic reconstruction is done by integrating the 4-D motion estimation into the tomographic projection operator matrix. Given a voxels set that discretizes the 3-D region of interest, the projection operator matrix coefficient $R_{p_n,k}$ encodes the contribution of voxel V_k to pixel p_n in image n . The solid angle with vertices the X-ray source at frame i and pixel p_n edges is denoted S_{p_n} .

In the static case, contributions are given by:

$$R_{p_n,k} = \text{vol}(S_{p_n} \cap V_k) \quad (1)$$

As shown in Figure 21, after a few calculations given in [BVMA03], the contribution in the dynamic case is obtained by:

$$R_{p_n,k}^\Phi = \text{vol}(S_{p_n} \cap \Phi_{t_n}(V_k)) \quad (2)$$

Finally, the exact contribution computation is approximated by single contributions and neglects the relative volume variation effect:

$$R_{p_n,k}^\Phi = \begin{cases} \text{vol}(V_k) & \text{if } \Phi_{t_n}(v_k) \in S_{p_n} \\ 0 & \text{else} \end{cases}$$

where v_k is the center of voxel V_k .

As the projection operator matrix R^Φ has been corrected for cardiac motion, we now can use an arbitrary tomographic reconstruction method. We chose the additive ART method [Her80]. The initial reconstruction is set to null intensity for all voxels, then an iterative update is done pixel-wise by additive distribution of the projection residuals for a given pixel. More precisely, if μ^l is a vector representing the current reconstruction, then the sum of contributions associated to pixel p_n in image n is given by $\langle R_{p_n,\cdot}^\Phi, \mu^l \rangle$, where $R_{p_n,\cdot}^\Phi$ is the raw of matrix R^Φ corresponding to pixel p_n contributions. The residual for pixel p_n

is thus given by $J_n(p_n) - \langle R_{p_n, \cdot}^\Phi, \mu^l \rangle$ and is homogeneously parted between contributing voxels: $\frac{J_n(p_n) - \langle R_{p_n, \cdot}^\Phi, \mu^l \rangle}{\|R_{p_n, \cdot}^\Phi\|^2} R_{p_n, \cdot}^\Phi$. The addition of a relaxation parameter $\lambda \in]0, 2[$ yields the following update scheme:

$$\mu^l \leftarrow \mu^l + \lambda \frac{J_n(p_n) - \langle R_{p_n, \cdot}^\Phi, \mu^l \rangle}{\|R_{p_n, \cdot}^\Phi\|^2} R_{p_n, \cdot}^\Phi$$

An iteration of ART algorithm is given by performing updates associated to all available pixels. In practice, we used 2 iterations of ART algorithm. Figure 22 presents comparative results for separate and combined effects of virtual subtraction and motion compensation on coronary arteries tomographic reconstruction.

3.4.3 4-D tomographic representation

the above tomographic reconstruction allows to estimate a 3-D image at one specific cardiac phase, which is chosen as the normalized cardiac time $t = 0$. Since a 4-D motion, $\Phi(\mathbf{p}, \cdot, \cdot)$, has been computed, it can be applied to this 3-D image as well to obtain a 3-D image at any arbitrary cardiac phase, yielding a 4-D tomographic representation.

This enables the visualization of the coronary tree geometry at an arbitrary cardiac phase, and from an arbitrary point of view. In particular, a simulated dynamic sequence (the coronary arteries under motion) can be rendered from an arbitrary point of view. Consequently, compared to the original rotational sequence, interesting additional information is available and a physician can visualize:

- the reconstruction from the same point than an original angiogram, but at a different cardiac phase and
- the reconstruction at the same cardiac phase than an original angiogram, but from the different point of view, including *mechanically non reachable* points of view such as in the axial direction.

Figure 23 exemplifies such visualization.

4 Results

We present some preliminary validation results obtained on a synthetic dynamic dataset and on patient datasets. Some potential clinical applications, enabled by the different stages of the proposed method, are also sketched.

4.1 Synthetic dynamic dataset

We successfully tested our tomographic reconstruction method on a synthetic dynamic dataset consisting in simulated angiograms observing nine cylinders with two different diameters, animated under a periodic homothetic dilatation/contraction motion. As presented

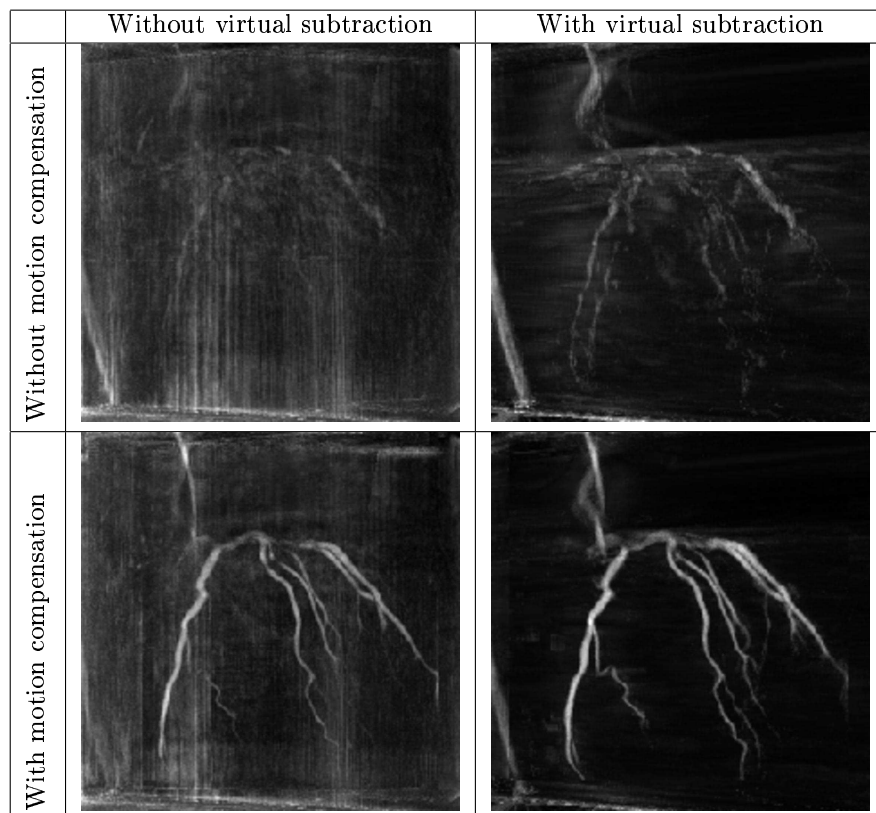


Figure 22: Separate and combined effects of virtual subtraction and motion compensation on coronary arteries tomographic reconstruction. MIP views in sagittal direction of four tomographic reconstructions obtained from the same original angiogram sequence, including or not virtual subtraction and motion compensation. Virtual subtraction removes background backprojection artifacts, while motion compensation drastically reduces cardiac motion blur artifacts.

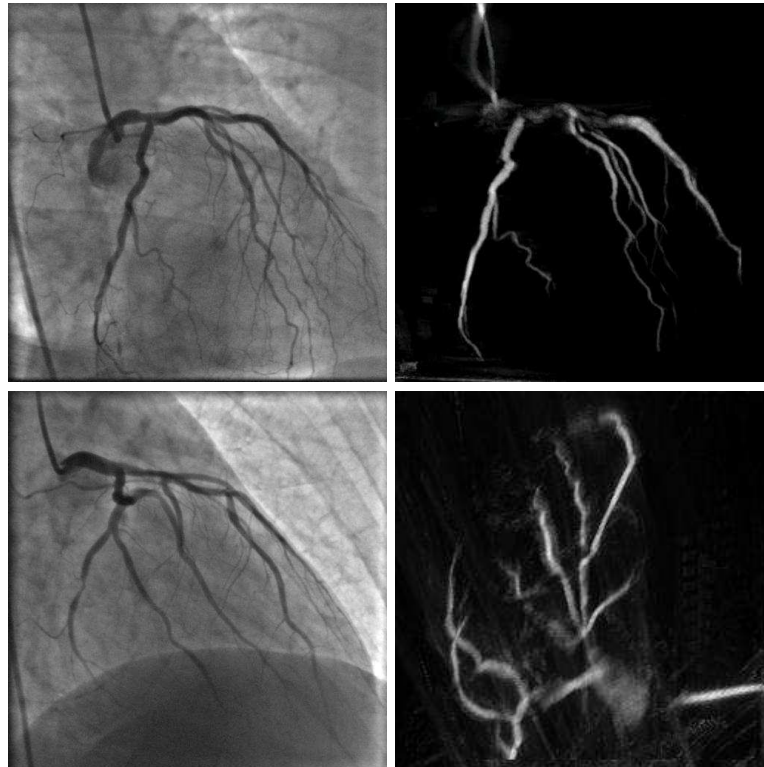


Figure 23: Application of 4-D tomographic representation. Top:(left) an original angiogram, and (right) the MIP view of the 4-D tomographic representation observed from the same point of view but at a different cardiac phase. Bottom: (left) an original angiogram, and (right) the MIP view of the 3-D tomographic reconstruction in axial direction: a mechanically non reachable point of view.

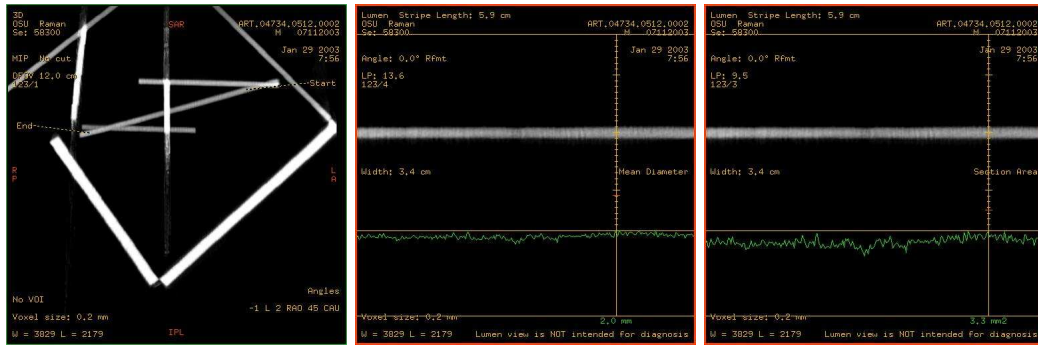


Figure 24: Comparison of ideal and measured diameters on a synthetic dynamic dataset. From left to right, definition of the start and end points of the cylinder of interest in the synthetic dynamic dataset reconstruction, mean diameter profile along cylinder axis gives 2.0 millimeters in average, and cylinder sectional area is 3.3 millimeters squared in average.

in Figure 24, we compared the measured cylinders diameters, obtained by the proposed tomographic reconstruction method, against the known diameters. While the ideal diameter is 2.0 millimeters, measured values are bounded between 1.9 millimeters and 2.1 millimeters and are 2.0 millimeters in average. The simple observed motion allowed an effective motion estimation by the proposed method, enabling an almost perfect tomographic reconstruction.

4.2 Patient datasets

We experimented our method on 16 patient datasets, that were qualified as either *good* or *medium* quality sequences, depending on visual characteristics such as:

- images contrast,
- sutures or highly contrasted non vascular structures presence, and
- angular rotation range.

We obtained sharp tomographic reconstructions for 80% of the good quality sequences and for 50% of the medium quality sequences.

We also assessed our reconstructions by comparing an object with known size, the catheter, and corresponding measures in the reconstruction. The known diameter value was 2.0 millimeters, while average measured value was 2.3 millimeters. Measure error was of the same order than voxel size (0.25 millimeter).

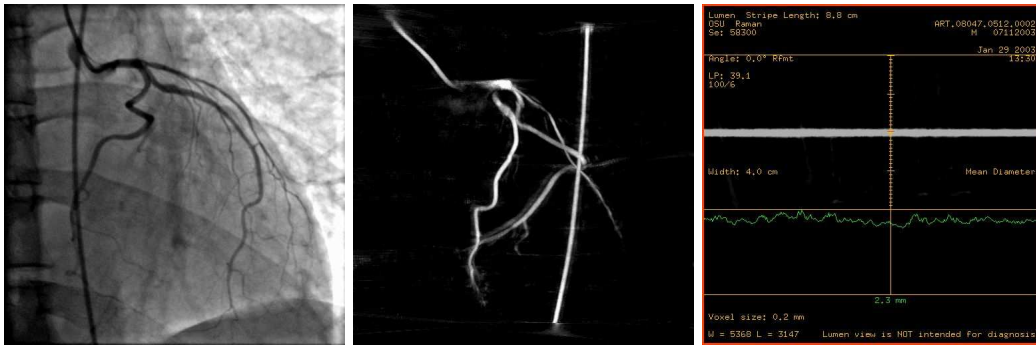


Figure 25: Comparison of known and measured catheter diameter. From left to right, original angiogram showing the catheter, tomographic reconstruction including a large part of the catheter. Mean diameter profile along catheter axis gives 2.3 millimeters in average while the true diameter is 2.0 millimeters.

4.3 Computational issues

For typical datasets, the data consists in 120 images at 512^2 spatial resolution, including 5 reference images. Our successive models have the following typical complexity:

- 2-D extracted centerlines represent 3 000 to 5 000 points per reference image,
- 3-D reconstructed centerlines count between 20 000 and 30 000 points after symmetrization, and 8 000 to 15 000 point after points fusion,
- 4-D motion has between 20 000 and 30 000 parameters, and
- 3-D tomographic reconstruction at 256^3 spatial resolution consists in more than 16 000 000 voxels.

It appears difficult to reduce the number of parameters of these models because of geometrical and dynamic complexity of coronary arteries and because of high inter-patient variability of the coronary artery tree.

As a results of the complexity of the models, computation times are important. On a Pentium 4 running at 2.4 GHz, first steps have the following computation time:

- multiscale filtering of the complete sequence takes 1 minute,
- 2-D centerlines extraction in the reference images takes 5 seconds, and
- 3-D centerlines reconstruction, including respiratory motion effect compensation, takes 10 to 50 minutes.

The next stages were parallelized using PVM [GBD⁺93], in order to drastically reduce the computation time. On 4 clustered workstations with 2 Xeon processors running at 2 GHz, last steps have the following computation time:

- 4-D motion takes 15 to 30 minutes and
- 3-D tomographic reconstruction takes 1 hour.

In summary, the total computation time is between 1.5 and 2.5 hours.

4.4 Potential clinical applications

Each of the different steps of the proposed method may induce potential clinical applications, that are briefly described below.

3-D centerlines reconstruction static 3-D centerlines reconstruction already contains information of interest. 1 Once a physician has clicked a point of interest in one of the reference angiograms, we can associate it to a 3-D point in the reconstructed centerlines. Then, we can compute many relevant informations:

- estimation of the magnification factor attached to the initial 2-D point,
- estimation of the optimal orientation of the acquisition system for a specific run, dedicated to lesion exploration [SAH98], and
- position of the corresponding point in the other reference angiograms and the corresponding magnification factor.

The latter item allows for instance to automatically repeat the 2-D QCA (Quantitative Coronary Analysis) procedure from distinct points of view, and consequently reduce the orientation dependence of the lesion assessment.

4-D motion on the physiological side, motion knowledge allows for detection of hypokinetic or akinetic parts of the myocardium, by extrapolating the 4-D motion we computed for coronary arteries motion. Identified regions may suffer from ischemia, possibly related to a coronary artery lesion.

On the visualization side, another application of 4-D motion estimation is the computation of a constantly focused and centered display of a region of interest during the rotational acquisition. This application, called *stabilized display*, has been detailed in [BMVA03]. It facilitates the mental tridimensional representation task for the physician by removing the need for eye-tracking the specific region of interest. Figure 26 illustrates the stabilized display tool.

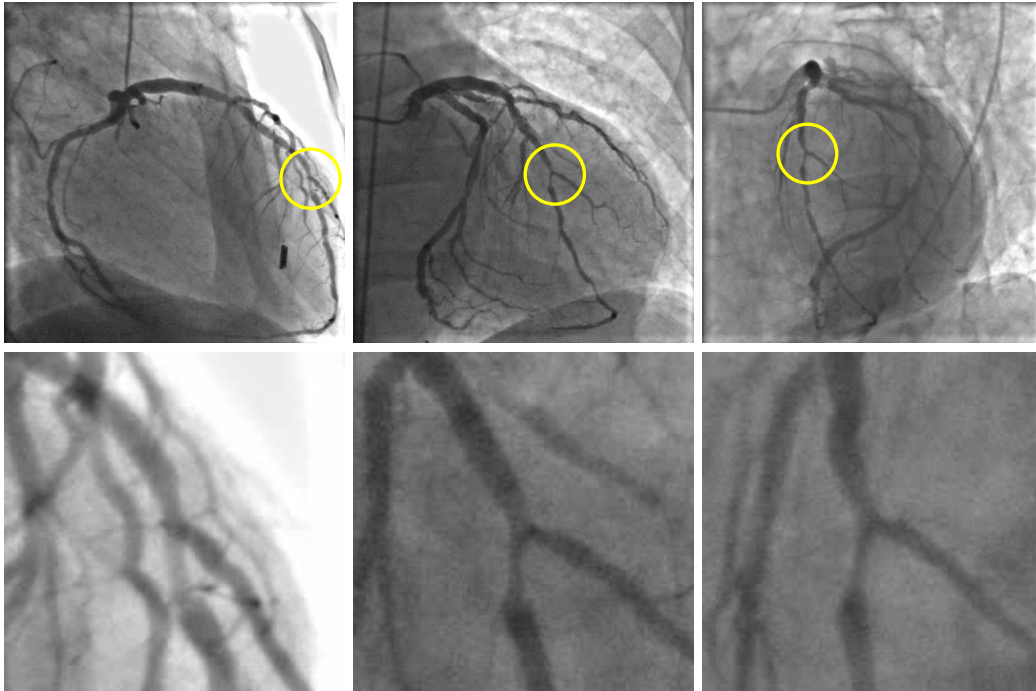


Figure 26: Stabilized display of a stenosis. Top: images that were acquired at distinct cardiac phases, from distinct points of view, in which we manually pointed the moving region of interest (a stenosis located at a bifurcation). Bottom: focused and automatically centered images around the region of interest in the same images.

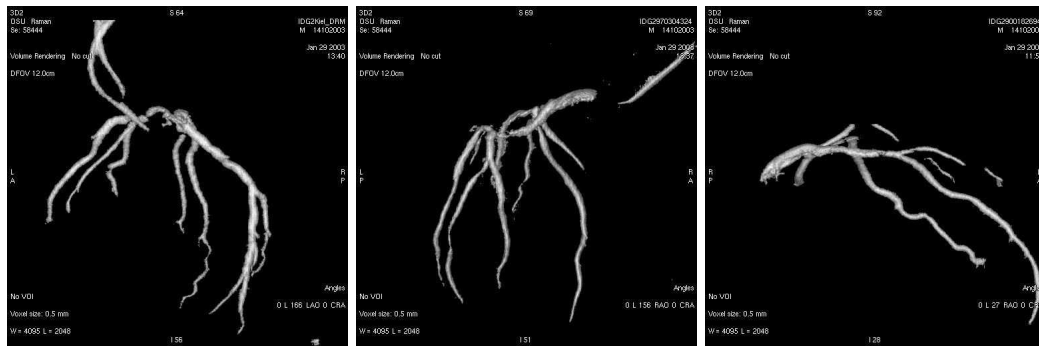


Figure 27: Isosurface views deduced from tomographic reconstructions obtained for three different patients, allowing for an easy mental handling of tridimensional coronary artery tree.

3-D tomographic reconstruction tomographic reconstruction have many clinical applications. Visualization tools can be derived from the reconstructions, for instance, we can provide physicians with:

- MIP (Maximum Intensity Projection) views,
- isosurface or level-set views, and
- endoluminal views.

As previously explained, these views present a 3-D tomographic reconstruction of coronary arteries from an arbitrary orientation and at an arbitrary cardiac phase. Figures 27 and 28 present examples of isosurface and endoluminal views, produced from 3-D tomographic reconstructions of coronary arteries.

These new visualization capabilities may help clinicians in mentally handling and representing the 3-D coronary vascular structure of a patient.

From a quantitative point of view, 3-D Quantitative Coronary Analysis is a promising tool. In this case, lesion severity would be characterized by an absolute vessel 2-D sectional area decrease, instead of the projected 1D diameter relative decrease that is proposed by current 2-D QCA clinical routine. In [BVMA04], we conducted a first test for 3-D Quantitative Coronary Analysis of a stenosis, which resulted in a 3-D characterization of stenosis severity. Clinical validation of 3-D Quantitative Coronary Analysis will be conducted within near future.

5 Conclusion

We presented a novel and stand-alone method to successively produce a 3-D reconstruction of coronary arteries centerlines, a 4-D motion estimation of coronary arteries, and a 3-D to-

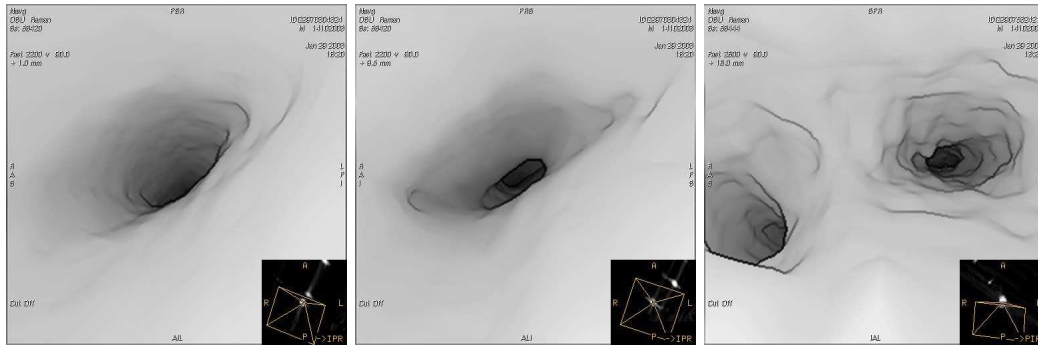


Figure 28: Endoluminal visualization of a 3-D tomographic reconstruction of coronary arteries. From left to right: endoluminal view in a normal artery, endoluminal view at a stenosis, and endoluminal view at a bifurcation. These views allow for easy in-vessel navigation and sectional profile visualization.

mographic reconstruction of coronary arteries from one single rotational X-ray acquisition. Obtained results, on both synthetic and clinical data, are really promising. In addition, potential clinical tools were described and prototyped.

Clinical validation of this work will be the subject of incoming studies, conducted in Hemodynamics and Interventional Cardiology Unit at Hospices Civils de Lyon, directed by Pr. Finet. Clinical validation will certainly result in identification of methodological improvement sources, including refinement of projection matrix operator computation, and in improvement of adequation between methods and imaging protocol, involving generalized acquisition trajectories study.

Acknowledgments

We gratefully thank clinicians who provided us with the patient rotational X-ray sequences (Doctors S.V. Raman, R.D. Magorien, and C.A. Bush from Ohio State University, at Columbus, United States of America, and Doctor W.R. Rüdiger Simon from Universitaetsklinikum, at Kiel, Germany). The authors thank Ève Coste-Manière for providing the Chir environment at INRIA, where part of this work was done, and Frédéric Devernay, from INRIA Rhône-Alpes, for fruitful discussions and technical knowledge sharing.

References

- [BKR⁺03] S. Bonnet, A. Koenig, S. Roux, P. Hugonnard, R. Guillemaud, and P. Grangeat. Dynamic X-ray computed tomography. *Proceedings of the IEEE*, 91(10):1574–1587, 2003. Emerging Medical Imaging Technology.

- [BMVA03] C. Blondel, G. Malandain, R. Vaillant, and N. Ayache. 4D Deformation Field of Coronary Arteries from Monoplane Rotational X-Ray Angiography. In *Proceedings of Computer Assisted Radiology and Surgery (CARS) 2003*, volume 1256 of *International Congress Series*, pages 1073–1078, Londres, June 2003. Elsevier.
- [BVD⁺02] C. Blondel, R. Vaillant, F. Devernay, G. Malandain, and N. Ayache. Automatic Trinocular 3D Reconstruction of Coronary Artery Centerlines from Rotational X-ray Angiography. In *Proceedings of Computer Assisted Radiology and Surgery (CARS) 2002*, pages 832–837, Paris, June 2002. Springer-Verlag.
- [BVMA03] C. Blondel, R. Vaillant, G. Malandain, and N. Ayache. 3D Tomographic Reconstruction of Coronary Arteries using a Precomputed 4D Motion Field. In Y. Bizais, editor, *Proceedings of the Seventh International Conference on Fully 3D Reconstruction In Radiology and Nuclear Medicine*, pages We AM 2–1, Saint-Malo, July 2003.
- [BVMA04] C. Blondel, R. Vaillant, G. Malandain, and N. Ayache. 3D tomographic reconstruction of coronary arteries using a precomputed 4D motion field. *Physics in Medicine and Biology*, 49(11):2197–2208, May 2004. Special Issue: Seventh International Meeting on Fully 3D Image Reconstruction in Radiology and Nuclear Medicine.
- [Dij59] E.W. Dijkstra. A note on two problems in connection with graphs. *Numerische Mathematik*, 1:269–271, 1959.
- [DSB⁺99] P.G. Danias, M. Stuber, R.M. Botnar, K.V. Kissinger, R.R. Edelman, and W.J. Manning. Relationship between motion of coronary arteries and diaphragm during free breathing: Lessons from real-time MR imaging. *American Journal of Roentgenology*, 172:1061–1065, 1999.
- [FNVV98] A.F. Frangi, W.J. Niessen, K.L. Vincken, and M.A. Viergever. Multiscale Vessel Enhancement Filtering. In W. Wells, A. Colchester, and S. Delp, editors, *Proceedings of Medical Image Computing & Computer Assisted Intervention (MICCAI) 1998*, volume 1496 of *Lecture Notes in Computer Science*, pages 130–137. Springer-Verlag, 1998.
- [GBD⁺93] A. Geist, A. Beguelin, J.J. Dongarra, W. Jiang, R. Manchek, and V.S. Sunderam. PVM 3 user’s guide and reference manual. Technical Report ORNL/TM-12187, Oak Ridge National Laboratory, 1993.
- [Gir87] G. Giraudon. An Efficient Edge Following Algorithm. In *Proceedings of 5th Scandinavian Conference on Image Analysis*, volume 2, pages 547–554, Stockholm, 1987.
- [GMW82] P.E. Gill, W. Murray, and M.H. Wright. *Practical optimization*. Academic Press, 1982.

- [Her80] G. Herman. *Image reconstruction from projections*. Academic Press, 1980.
- [HGE98] A.E. Holland, J.W. Goldfarb, and R.R. Edelman. Diaphragmatic and cardiac motion during suspended breathing: Preliminary experience and implications for breath-hold MR imaging. *Radiology*, 209(2):483–489, November 1998.
- [KGYF02] J. Keegan, P. Gatehouse, G.Z. Yang, and D. Firmin. Coronary artery motion with the respiratory cycle during breath-holding and free-breathing: implications for slice-followed coronary artery imaging. *Magnetic Resonance in Medicine*, 47:476–481, 2002.
- [KMA⁺00] K. Krissian, G. Malandain, N. Ayache, R. Vaillant, and Y. Troussel. Model-based detection of tubular structures in 3D images. *Computer Vision and Image Understanding*, 80(2):130–171, 2000.
- [KND02] E. Kuon, P.N. Niederst, and J.B. Dahm. Usefulness of Rotational Spin for Coronary Angiography in Patients with Advanced Renal Insufficiency. *American Journal of Cardiology*, 90(4):369–373, August 2002.
- [LT01] C.T. Lawrence and A.L. Tits. A Computationally Efficient Feasible Sequential Quadratic Programming Algorithm. *SIAM Journal on Optimization*, 11(4):1092–1118, 2001.
- [LZT97] C. Laurence, J.L. Zhou, and A.L. Tits. *User's Guide for CFSQP Version 2.5: A C Code for Solving (Large Scale) Constrained Nonlinear (Minimax) Optimization Problems, Generating Iterates Satisfying All Inequality Constraints*. University of Maryland, 1997.
- [MFLM98] A.B. Merle, G. Finet, J. Liénard, and I.E. Magnin. 3D reconstruction of deformable coronary tree skeleton from two x-ray angiographic views. In *Proceedings Computers in Cardiology*, pages 775–760, Cleveland, Ohio, September 1998. IEEE.
- [MRV⁺03] B. Movassaghi, V. Rasche, M.A. Viergever, W. Niessen, and R. Florent. 3D coronary reconstruction from calibrated motion-compensated 2D projections. In *Proceedings of Computer Assisted Radiology and Surgery (CARS) 2003*, volume 1256 of *International Congress Series*, pages 1079–1084. Elsevier, June 2003.
- [RAH97] P. Radeva, A. Amini, and J. Huang. Deformable B-solids and implicit snakes for 3D localization and tracking of SPAMM MRI data. *International Journal of Computer Vision and Image Understanding*, 66:163–178, 1997.
- [RBCC94] R. Ruan, A. Bruno, R. Collorec, and J.L. Coatrieux. 3D motion and reconstruction of coronary arteries from biplane cineangiography. *Image and Vision Computing*, 12(10):683–689, 1994.

- [RGK⁺02] V. Rasche, M. Grass, R. Koppe, A. Bücke, R. Günther, H. Köhl, J. Op de Beek, R. Bertrams, and R. Suurmond. ECG-gated 3D rotational coronary angiography. In *Proceedings of Computer Assisted Radiology and Surgery 2002*, pages 826–831, Paris, 2002. Springer-Verlag.
- [RMV⁺02] S.V. Raman, R.D. Magorien, R. Vaillant, P. Payne, K. Benali, and C.A. Bush. Rotational Cardiovascular X-Ray Imaging for Left Coronary Artery Angiography Using a Digital Flat-Panel Cardiac Imaging System. *American Journal of Cardiology*, 90(6A), 2002.
- [SAH98] T. Sato, T. Araki, and M. Hanayama. A viewpoint determination system for stenosis diagnosis and quantification in coronary angiographic image acquisition. *IEEE Transactions on Medical Imaging*, 17(1):121–137, February 1998.
- [SDQ⁺03] G. Shechter, F. Devernay, A. Quyyumi, È. Coste-Manière, and E.R. McVeigh. Three-Dimensional Motion Tracking of Coronary Arteries in Biplane Cineangiograms. *IEEE Transactions in Medical Imaging*, 22(4):493–603, April 2003.
- [Ser82] J. Serra. *Image analysis and mathematical morphology*. Academic Press, 1982.
- [SNS⁺98] Y. Sato, S. Nakajima, N. Shiraga, H. Atsumi, S. Toshida, T. Koller, G. Gerig, and R. Kikinis. 3D multi-scale line filter for segmentation and visualization of curvilinear structures in medical images. *Medical Image Analysis*, 2(2):143–168, June 1998.
- [Van73] G.N. Vanderplaats. *CONMIN - A ForTran program for constrained function minimization - User's manual*. NASA, 1973. Technical Memorandum X-62,282.
- [WRE95] Y. Wang, S.J. Riedere, and R.L. Ehman. Respiratory Motion of the Heart: Kinematics and the Implications for the spatial resolution in coronary imaging. *Magnetic Resonance in Medicine*, 33(5):713–719, May 1995.



Unité de recherche INRIA Sophia Antipolis
2004, route des Lucioles - BP 93 - 06902 Sophia Antipolis Cedex (France)

Unité de recherche INRIA Futurs : Parc Club Orsay Université - ZAC des Vignes
4, rue Jacques Monod - 91893 ORSAY Cedex (France)

Unité de recherche INRIA Lorraine : LORIA, Technopôle de Nancy-Brabois - Campus scientifique
615, rue du Jardin Botanique - BP 101 - 54602 Villers-lès-Nancy Cedex (France)

Unité de recherche INRIA Rennes : IRISA, Campus universitaire de Beaulieu - 35042 Rennes Cedex (France)

Unité de recherche INRIA Rhône-Alpes : 655, avenue de l'Europe - 38334 Montbonnot Saint-Ismier (France)

Unité de recherche INRIA Rocquencourt : Domaine de Voluceau - Rocquencourt - BP 105 - 78153 Le Chesnay Cedex (France)

Éditeur
INRIA - Domaine de Voluceau - Rocquencourt, BP 105 - 78153 Le Chesnay Cedex (France)
<http://www.inria.fr>
ISSN 0249-6399